Received: 8 July 2021 | Revised: 1 December 2021 | Accepted: 18 January 2022
DOI: 10.1002/tal.1924

RESEARCH ARTICLE

WILEY

Experimental study and numerical simulation of all-steel buckling-restrained brace with distributed inspection windows

Chunfeng Wan[1] | **Liyu Xie**[2] | **Lin Li**[2,3] | **Songtao Xue**[2,4] | **Hesheng Tang**[2] | **Li Zhang**[2]

[1]Key Laboratory of Concrete and Pre-Stressed Concrete Structure of Ministry of Education, Southeast University, Nanjing, China

[2]Department of Disaster Mitigation for Structures, Tongji University, Shanghai, China

[3]Southwest Electric Power Design Institute, Chengdu, China

[4]Department of Architecture, Tohoku Institute of Technology, Sendai, Japan

Correspondence
Liyu Xie, Department of Disaster Mitigation for Structures, Tongji University, Shanghai 200092, China.
Email: liyuxie@tongji.edu.cn

Funding information
Intergovernmental International Scientific and Technological Innovation Cooperation Special Focus, Grant/Award Number: 2021YFE0112200; Natural Science Foundation of Shanghai, Grant/Award Number: 20ZR1461800

Summary

This paper presents a novel all-steel seismic-resistant, buckling-restrained brace (BRB) which can be easily detached from its steel core for post-seismic inspections. This allows inspectors to quickly determine if the BRB needs to be replaced to reduce the impact of seismic aftershocks. The weld toes of brace stiffeners were specially smoothed to reduce the residual stress and stress concentration, thereby improving the low-cycle fatigue performance of the brace. Two identical restraining units were connected by high-strength bolts. A small air gap was provided by annular gaskets between the core and the restraining system to allow for lateral expansion of the core plate under compression. Five specimens were tested under different cyclic loading protocols to investigate the performance. The hysteretic behavior, compression strength adjustment factor, equivalent viscous damping ratio, failure modes, and deformation of the restraining system were analyzed. The multi-wave buckling deformation of the core was studied in detail to provide a basis for the accurate calculation of the number of contact points. Finite element analyses were performed to compare the response with test results, which proved the structure of the novel BRB to be reasonable except for the compression strength adjustment factor of some specimens, which was greater than 1.3. A damage assessment method was proposed to evaluate the working status of the newly designed BRB after an earthquake.

KEYWORDS
all-steel assembly, buckling-restrained brace, damage assessment, inspectable core, multi-wave deformation, seismic-resistant

1 | INTRODUCTION

Shortly after Japan's magnitude-9 earthquake and tsunami in March 2011, the Japan Society of Seismic Isolation (JSSI) investigated the condition of passive-controlled structures, including buildings with base isolation and supplemental damping devices. No superstructure failures were reported, but numerous failures of expansion joints were found and significant failures of lead dampers for base-isolated buildings were investigated and reported.[1] Kasai et al.[2] further confirmed the damage by reporting cracks in lead dampers for the base-isolated buildings as a result of this earthquake. Xie et al.[3] reported that the oil dampers of an eight-story steel building were destroyed during the 2011 Great East Japan Earthquake and concluded that the insufficient stroke limit caused the pounding between the dampers and the abutments on the floor and subsequently damaged the dampers. Cao et al.[4] proposed a hybrid retrofit using tin-rubber bearings to replace the damaged oil damper of this building.

The actual seismic hazards showed that the dampers were likely to be damaged or destroyed in strong earthquakes. After an earthquake, it is necessary to assess the state of dampers to determine if they should be replaced to ensure the seismic load capacity of the structures they

https://doi.org/10.1002/tal.1924

support. The buckling-restrained brace (BRB) has been widely used as an effective metal damper for engineering structures located in high seismic intensity areas.[5,6] This BRB not only provides support for the lateral stiffness of the structure but also dissipates the seismic energy through axial plastic deformation to protect the main structure much like a fuse. However, BRBs must still be evaluated after an earthquake to determine the safety of a structure and the need to replace the damaged BRB. In contrast to a general steel brace, a BRB is composed of an inner core and a restraining system. In principle, the axial force is only sustained by the inner core. When the inner core is pressed, the restraining system can limit the oversized lateral deformation of the inner core, so the high-order buckling deformation only occurs in the cavity of the restraining system. A BRB yields without buckling under an axial compression load and provides a good hysteretic response and energy dissipation capacity. However, since the inner core is surrounded by the restraining system, the deformation or damage state of the inner core cannot be determined after the earthquake.

At present, commonly used BRBs are divided into three types based on different restraint methods: (1) the steel and concrete integral, (2) the all-steel integral, and (3) all-steel assembled BRB. The steel core and concrete integral BRB is constrained by steel members filled with concrete or mortar; moreover, its core surface requires additional debonding material to prevent cohesive force between the concrete and the core. Numerous tests have been carried out on steel and concrete integral BRBs.[7–13] The results showed that the hysteretic responses were stable, but the concrete or mortar was easily crushed under cyclic loading, which eliminated effective constraint on the core. Moreover, the concrete pouring process is complex, and the quality is not easily controlled.[14]

Based on the shortcomings of the steel and concrete integral BRB, an all-steel integral was proposed in which the core is restrained by a single steel member or welded steel members. Many scholars have conducted experimental research on this steel core/steel members restraint concept.[15–19] Test results have shown that the hysteretic performance and low-cycle fatigue properties were excellent if the detail construction was reasonable. Because there is no cohesive force between the inner core and the restraining system, debonding material may not be provided in construction. The all-steel integral BRB has the advantages of good mechanical properties, convenient manufacturing, and light weight, which has been applied more and more.[20]

The restraining system of an integral BRB is a whole, and the yield segment of the core is surrounded by the restraining system. After an earthquake, it is difficult to quickly assess the deformation state of the BRB core, and it is impossible to efficiently and effectively determine the need for replacement. Furthermore, the restraining system cannot be reused after brace failure. Therefore, the all-steel assembled BRB is a viable option which can solve the above problem. Many types of all-steel assembled BRBs have been studied,[21–27] and their performance has not been any worse than integral BRBs. The restraining system of an all-steel assembled BRB is composed of several restraining units connected by bolts, and the gap between restraining units is fixed by a longitudinal pad strip. After an earthquake, it is necessary to remove the bolts to determine the deformation state of the core; however, this process is very troublesome, and it is difficult to reinstall accurately after disassembly. Liu and Tsai[28] set observation windows on the surfaces of the restraining system, through which they could determine the deformation state and fracture location of the core. But observation windows cannot be distributed along the whole length of the brace. Only local segments can be observed.

After an earthquake, it is necessary to evaluate the working state of the BRB to determine if the BRB should be replaced and to reevaluate the bearing capacity of the structure. Takeuchi et al.[29] proposed a deterministic fatigue model for predicting the cumulative deformation and energy absorption capacities of BRBs under random amplitudes, which requires knowledge of the BRB force-deformation histories. Andrews et al.[30] developed ductility capacity models for BRBs using a statistical framework and the results of past experimental studies. Their model can be used to predict BRB failure in engineering applications with sufficient accuracy. In addition, most models require knowledge of BRB imposed deformation histories. These BRB capacity evaluation models are computationally complex. This research used the Park–Ang[31] damage model to assist in the process of post seismic damage assessment in the BRB development proposed here.

Based on the previous research results, an all-steel assembled BRB with distributed inspection windows on the side was proposed in this paper. The deformation state of the core can be inspected from the BRB side without disassembling the restraining system. Because the normal contact force between the core and the restraining system has a great influence on the local strength of the restraining member, additional research focused on the multi-wave buckling deformation of the core. The performance of the inspection-ready BRB was verified by experiments and finite element (FE) analysis. A test program for five specimens is described in this paper, and the results are presented. Nonlinear FE analyses using ABAQUS were carried out in detail to compare the load-deformation hysteretic curves and the multi-wave buckling deformation. Moreover, the influence of friction was simulated as well as the maximum equivalent plastic compressive strain of the core.

2 | TEST PROGRAM

2.1 | Detailing of the BRB

Five BRB specimens were designed for testing. The five specimens were identical in all details except for the cyclic loading protocols. The viewable all-steel assembled BRB consists of core, stiffeners, panels, channels, annular gaskets, high-strength bolts, limit grooves, and end plates. The details of different parts of the BRB are illustrated in Figure 1.

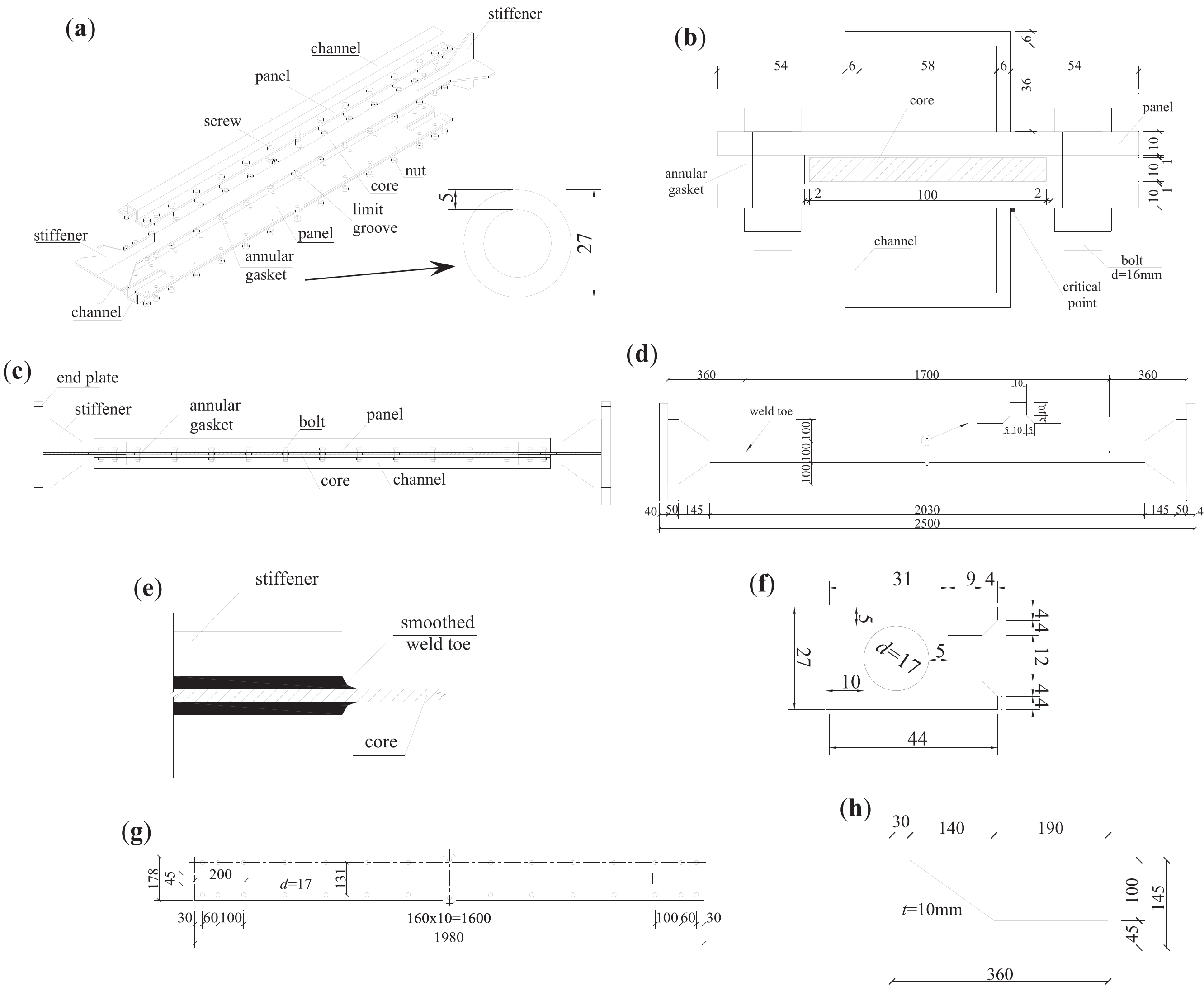

FIGURE 1 Detailing of the inspection-ready all-steel assembled BRB: (a) axonometric drawing; (b) cross-section view; (c) side view; (d) detailing of the core; (e) smoothed weld toe; (f) limit groove; (g) detailing of the panel; (h) detailing of stiffener

2.1.1 | Core

A flat shape is usually selected for the core due to its better fatigue behavior in comparison with a welded cruciform section,[25] and it is easy to manufacture. Hence, a 100 × 10 mm plate made of Chinese Q235-B grade steel with a nominal yield strength of 235 MPa was used for the core. As shown in Figure 1c, the core end section is enlarged, and the stoppers were set at the center by enlarging the width of the core plate to allow insertion into the limit grooves. The distances between the two end plates and the restraining system are equal; which provides a symmetric condition for the two ends of the core. The forming of the core requires a smooth cutting process and meticulous quality control.

The ends of core were reinforced by stiffeners to prevent premature damage to the BRB ends. The length of the stiffeners extending into the restraining members was 170 mm. As such, the yield length of the core was 1700 mm, and the total length of the core was 2420 mm, considering the yield part and stiffened segments. The total length of the brace was 2500 mm and end plates were included. The stiffeners and the ends of the core were connected in the form of fillet welds, which are used to reduce residual stress and stress concentration at the weld toes. Fracture may initiate at the intersection points of stiffeners and the core, so the low-cycle fatigue performance and the plastic deformation capability can be reduced. Notably, the influence of the weld toes on the BRB low-cycle failure could not be quantified, although the tensile fracture of the core was observed because of the welds between the stiffeners and the yield portion of the core.[20,27,32] To improve the low-cycle fatigue performance of the BRB, the weld toes of the stiffeners were specially smoothed, as shown in Figure 1e.

Uniaxial tensile tests were conducted on three coupons taken from the same plate of steel as the core, the coupons were cut parallel to the longitudinal direction of the core. From the test results, the average values of elastic modulus, yield strength and elongation for Q235-B were

187 GPa, 282 MPa and 0.295. The deformation ability of the material was fine, which satisfied the requirement of material performance for BRB. By multiplying the yield strength of the core plate by its cross section, the brace yield force was 282 kN.

Two 450 × 450 × 40 mm end plates were used to transfer the load to the core. Fillet welds connected the core and stiffeners to the end plates. Each end plate was connected to test equipment with four high-strength Chinese grade 8.8 bolts with diameter of 42 mm. The thickness of end plates was 40 mm, which was selected in such a way as to make the plate stiff enough to prevent out-of-plane deformation.

2.1.2 | Restraining system

The restraining system consisted of two restraining units and was checked to satisfy the design criteria[14] for preventing global buckling of the brace. The restraining unit was a 178 × 10 mm panel and was reinforced by a channel steel structural section of 70 × 42 × 6 mm for out-of-plane stability. Channels and panels made of Chinese Q345-B grade with a nominal yield strength of 345 MPa and were connected by fillet welds. In order to provide space for the displacement of stiffeners, the panel ends were grooved. The length of these grooves was longer than half of the maximum compressive displacement, and the grooves were made wider than the thickness of the stiffeners to compensate for the construction tolerance and to avoid friction between panels and stiffeners.

Two restraining units were connected together through corresponding annular gaskets with hand tightened Chinese grade 8.8 bolts with a diameter of 16 mm. The spacing and number of bolts were determined by normal force of contact points between the core and restraining units, and were also controlled by the local strength of the restraining units within a span equal to bolt spacing. Under the action of normal force, it was necessary to calculate the local strength along the longitudinal and transverse direction. The longitudinal bending demand was evaluated by assuming a point load in the middle of a simply supported beam with a span equal to the bolt's longitudinal spacing, while the transverse bending demand was estimated by assuming a uniform line load to a simply supported beam with a span equal to the transverse distance of the two bolted columns. The longitudinal distance of the adjacent bolt was 160 mm. To avoid the premature failure of the ends, the distance between the end bolts was reduced appropriately, as shown in Figure 1g.

A minimum clearance was needed to allow for expansion of the core due to the Poisson effect to avoid the excessive friction between the core and restraining system. However, if adequate clearance is provided between the core and restraining system, the normal force acting on the restraining system rises and the compression-bearing capacity declines as the clearance increases. In this study, the restraining system was designed to provide a 2-mm gap through the core thickness and a 4 mm gap through core width to allow for expansion in compression cycles. Since there was no cohesive force between the core and restraining system, no lubrication material was provided.

2.2 | Test setup and testing protocol

Five identical specimens were subjected to the quasi-static cycle tests with five different loading protocols, as shown in Figure 2. The cyclic axial displacements were applied along the BRB axis. It was assumed that the deformation concentrated in the yield region. The standard loading protocol was based on American Institute of Steel Construction (AISC) Seismic Provisions for Steel Buildings.[33]

At the beginning of each loading protocol, four cycles of loading with a strain amplitude of $\Delta\varepsilon^{+} = \Delta\varepsilon^{-} = 0.5\varepsilon_y$ were adopted to measure the initial axial stiffness of all specimens within an elastic stage and to examine the loading system. The standard loading protocol consists of two cycles at a deformation corresponding to the first significant yield point of the specimen, Δb_y followed by two cycles at each peak of 0.5, 1.0, 1.5, and 2.0 times the deformation corresponding to the design story drift (not less than 0.01 times the story height), Δb_m. The subsequent loading phase of the standard loading protocol was additional cycles at 1.5 times the deformation corresponding to the design story drift. The deformation Δ_{by} can be calculated from the yield force of the core and its axial stiffness, regardless of the deformation of transition segments considering that the axial stiffness of the transition segment is much larger than the core. So the first significant yield point Δ_{by}, can be calculated as follows:

$$\Delta_{by} = \frac{F_y}{EA/L_y} = \frac{282000}{187000 \times 1000/1700} = 2.5\text{mm}. \tag{1}$$

The brace deformation corresponding to the design story drift was related to the mounting angle, the length ratio of the yield segment, and the contribution of the surrounding frame members to the lateral stiffness.[21] The results showed that the strain demand of the core yield segment was usually between 1% and 2% unless the length of core was very short and the strain can reach 3%–5%.[25] In this study, the strain demand of the core yield segment corresponding to the design story drift was 1%. Specimen 1 was subjected to constant amplitude cyclic loading, and the core strain amplitude was equal to 1.5%. Specimen 2 underwent the standard loading protocol. Specimen 3 testing was conducted by applying the cyclically decreasing strain, starting from 2.0% to 0.5% with a decrement of 0.5%, followed by constant amplitude cycle. The loading protocols from Specimens 1 to 3 were symmetric, Specimens 4 and 5 were asymmetric. Specimens 4 and 5 were tested asymmetrically towards

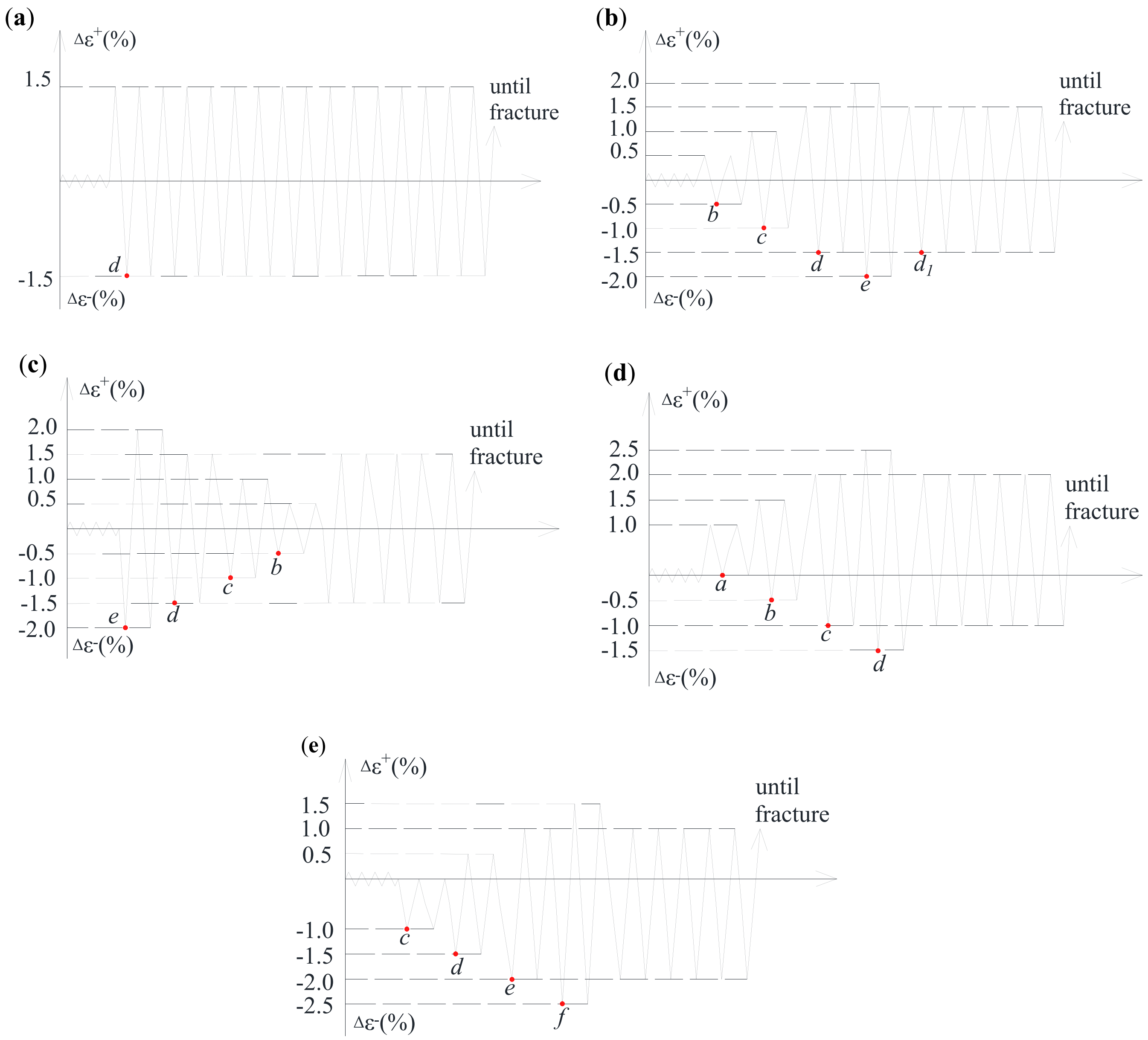

FIGURE 2 Five different loading protocols: (a) IBRB1; (b) IBRB2; (c) IBRB3; (d) IBRB4; (e) IBRB5

the tension and compression side, respectively, based on the standard loading protocol, to the extent of 0.5%. Moreover, all the loading protocols were continued until the failure of the specimens. Specimens 3 and 5 tests were conducted with the compressive strain applied first, while the other specimens were subjected to the tensile strain first in a cycle. During the tests, the actuator loading was held at each first compressive strain peak to record the high-mode buckling wave shapes. The monitoring points (a–e) are shown in Figure 2.

The axial force was measured by a load cell in the horizontal test setup, as shown in Figure 3. During the test, a total of six linearly variable displacement transducers (LVDTs) were installed on the specimens, as shown in Figure 4. The relative axial displacement of the two end plates was monitored by two LVDTs (LVDT1 and LVDT2) and the average amount was considered as the value of displacement controlled loading. Moreover, two other LVDTs measured the distance between the restraining system and the end plates at the left (LVDT3) and at the right (LVDT4) of the specimen to check the stopping mechanism and the slippage of the restraining system. Two LVDTs were mounted to monitor the potential lateral deformation of the specimen, along the thickness and width direction of the core (LVDT5 and LVDT6). Six strain gauges (Figure 3) were glued to the left, middle, and right of the restraining system to measure the contribution of the restraining system in load carrying and to also monitor its local performance and probable damage. Three strain gauges were installed in the middle of the channel web, and the other three were mounted on the panel near the critical point. Each strain gauge can measure the strain of the restraining system along the longitudinal and transverse directions. All the data was collected every second using a digital data acquisition system. The details of the specimen are shown in Figure 5.

3 | EXPERIMENTAL RESULTS AND DISCUSSION

3.1 | Hysteretic loops

The hysteretic loops of the five specimens were presented in Figure 6, where the failure point of each specimen is marked with a circle. In the figures, the horizontal axis is the average displacement measured by LVDT1 and LVDT2, while the vertical axis was the reaction force exerted by the actuator, where the tension was positive, and the compression was negative. Meanwhile, the number of cycles at the moment of failure

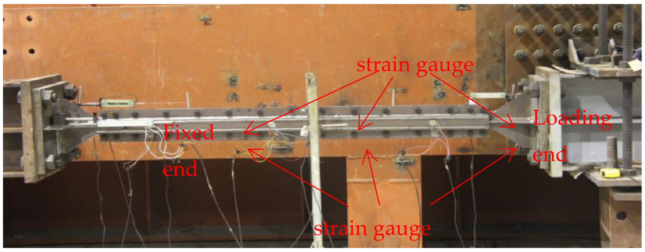

FIGURE 3 Test setup

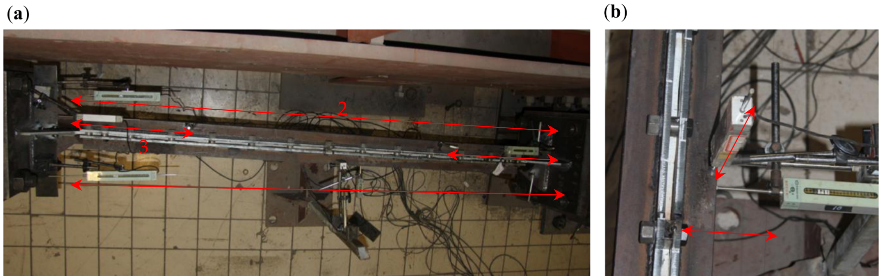

FIGURE 4 Layout of LVDTs: (a) LVDT1-4; (b) LVDT5-6

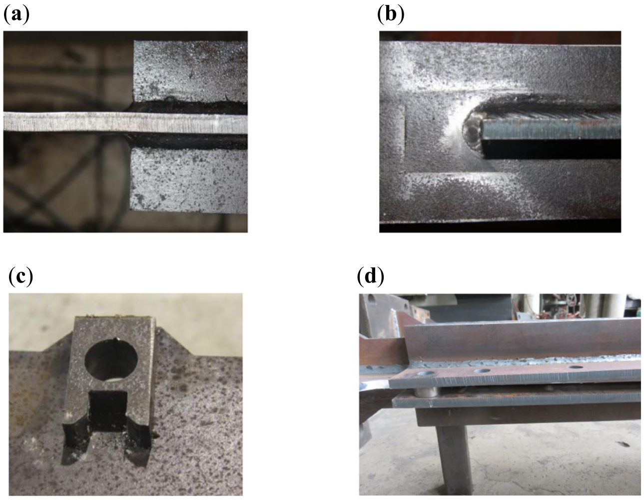

FIGURE 5 Details of the specimen: (a) smoothed weld toe; (b) smoothed weld toe from side view; (c) limit groove; (d) end of brace

during the constant strain amplitude (CSA) loading was plotted in the lower right corner of the figures, including the unfinished cycle. It can be seen in Figure 6 that the values of the parameters N_CSA for different specimens are quite different under the same CSA loading. This behavior is caused by the different loading histories for different specimens, which can lead to different plastic deformation accumulations before CSA loading.

All the specimens exhibited stable hysteretic behavior without degradation of the bearing capacity. The hysteretic loops of the second cycle at each displacement amplitude embraced the first cycle which was the result of the isotropic hardening of steel combined with the frictional cumulative effect. The specimen tests were successfully completed without global instability, local instability, weld crack, and bolt looseness. The cumulative plastic ductility (CPD) capacities for Specimens 1 to 5 were 571, 476, 533, 402, and 300 times the yield axial deformation, respectively. Thus, all exceeded the AISC CPD requirement that the brace test specimen achieve a cumulative inelastic deformation of at least 200 times the yield deformation (exceeding the CPD of 200).[33]

Ideally, the displacement of LVD3 (L3) and L4 should be equal, but the results showed that the two were not equal, as shown in Figure 7. The relationship between L3 + L4 and (L1 + L2)/2 is shown in Figure 8, which is basically equal, indicating that the measurement results are reliable. This difference may be due to the considerable friction that was uncertain and complex, resulting in uneven axial deformation of the core. Here, Specimen 4 was taken as an example, and the results of other specimens were consistent.

3.2 | The compression strength adjustment factor

As shown in Figure 6, the maximum compressive bearing capacity was greater than the maximum tensile bearing capacity under a certain cycle due to the Poisson effect and the frictional force between the core and the restraining system. Much less friction occurs when the BRB can sustain tension, which allows the reaction force in compression and tension to become more asymmetrical. The compression strength adjustment factor β was defined as

$$\beta = \frac{C_{peak}}{T_{peak}}, \tag{2}$$

where C_{peak} and T_{peak} are respectively the ultimate forces in compression and tension for each cycle.

The experimental β values for all the five specimens at different strain levels or CPD values are plotted in Figure 9.

Specimen 1 had a CSA cyclic loading with a strain amplitude equal to 1.5%. In the first cycle, the β value was relatively high owing to the cyclic hardening effect under the large strain amplitude, where the cyclic stress amplitude increased considerably with the loading history until the formation of a stable hysteretic loop.[34] Therefore, the β value of the first cycle was equal to 1.46, which was not entirely caused by the Poisson effect and the friction effect and cannot represent the true sense of β. After that, the β values were relatively stable with little fluctuation, and the maximum value of the β values was 1.28, which was less than the recommended limit value of 1.3 based on AISC specifications.[33]

Specimen 2 was conducted according to the standard loading protocol. Thus, the incremental strain amplitude (ISA) loading was carried out followed by CSA loading. Because of the small strain applied in the first cycle, the cyclic hardening effect was not as obvious as that of Specimen 1. During the ISA loading, β values increased with the increase of compressive strain. In general, the β values of the second cycle at each strain amplitude were less than that of the first cycle, possibly due to the change in smoothness of the contact surfaces. The maximum β value of the ISA loading phase was 1.40 greater than 1.30 specified by AISC.[33] During the CSA loading phase, the β values increased steadily, and the maximum value was 1.26.

Specimen 3 was loaded based on the decreasing strain amplitude (DSA) followed by CSA loading. Specimen 3 testing was conducted with the maximum compressive strain applied first. At this time, the first-cycle β value is usually less than 1.0 due to the cyclic hardening effect. If no friction exists, the value may be smaller. When the hysteretic curve was stable, the β values decreased as the peak compressive strain decreased. The maximum value of the DSA loading phase was 1.32, which is slightly greater than the 1.30 specified by AISC.[33] During the CSA loading phase, the β values increased steadily, and the maximum value was 1.24.

Specimen 4 was tested cyclically towards the tension side based on the standard loading protocol. The maximum tensile strain under a certain cycle was 1.0% greater than the maximum compressive strain, so the ratio of the maximum compressive force to the maximum tensile force was smaller than the β value of symmetric loading. To facilitate analysis efficiency, this ratio was calculated using Equation 1. The maximum β value of the ISA loading phase was 1.28, and the maximum β value of the CSA phase was 1.23.

Specimen 5 was executed cyclically towards the compression side based on standard loading protocol. The specimen fractured during the first cycle of the CSA loading phase. The maximum tensile strain under a certain cycle was 1.0% less than the maximum compressive strain, so the ratio of the maximum compressive force to the maximum tensile force was greater than the β value of symmetric loading. Like Specimen 4, the ratio of the maximum compressive force to the maximum tensile force was still calculated by Equation 1. The maximum β value of the whole loading phase was 1.36. However, the β value of the second cycle was greater than that of the first cycle at each strain amplitude.

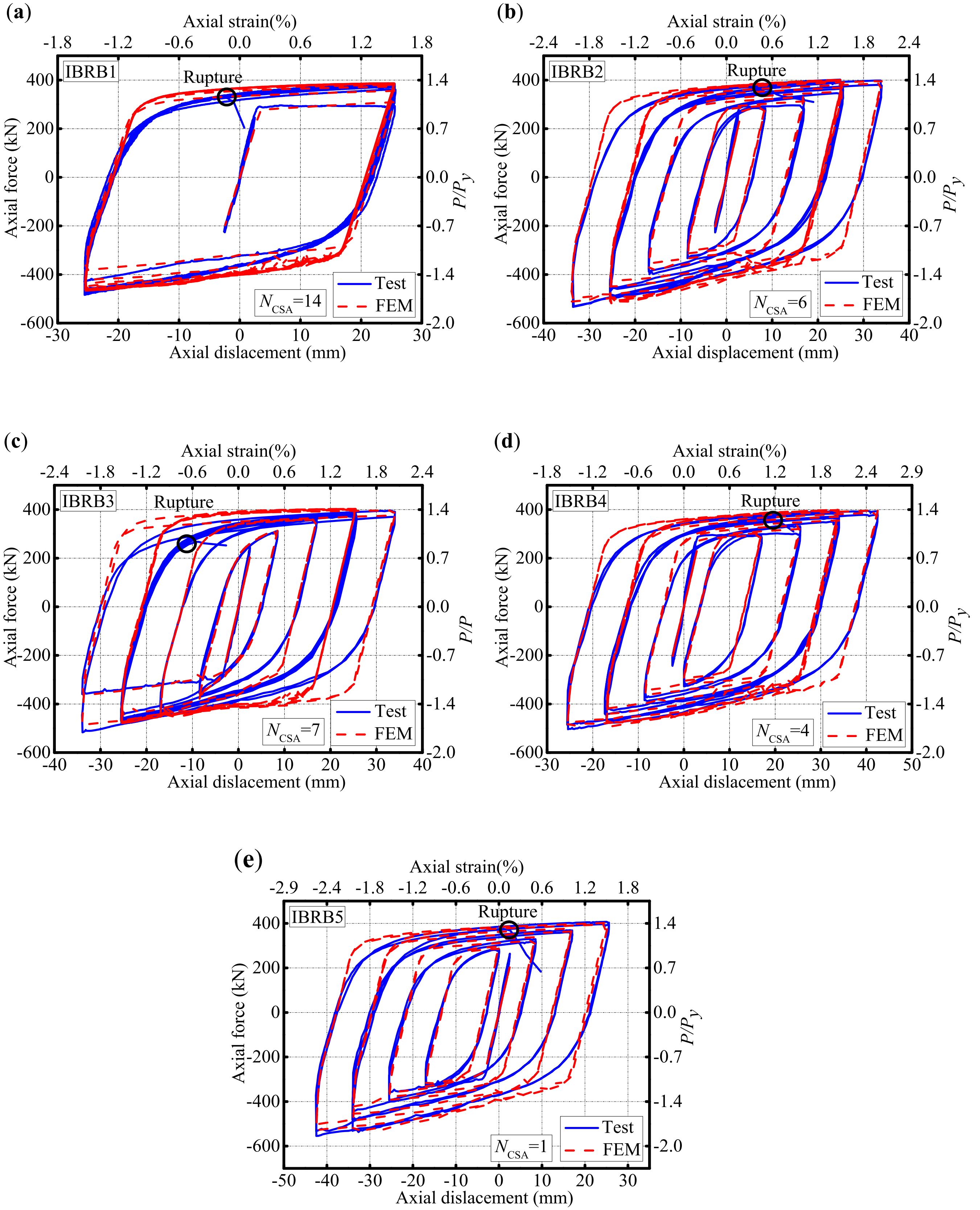

FIGURE 6 Axial force versus displacement of specimens: (a) Specimen 1; (b) Specimen 2; (c) Specimen 3; (d) Specimen 4; (e) Specimen 5

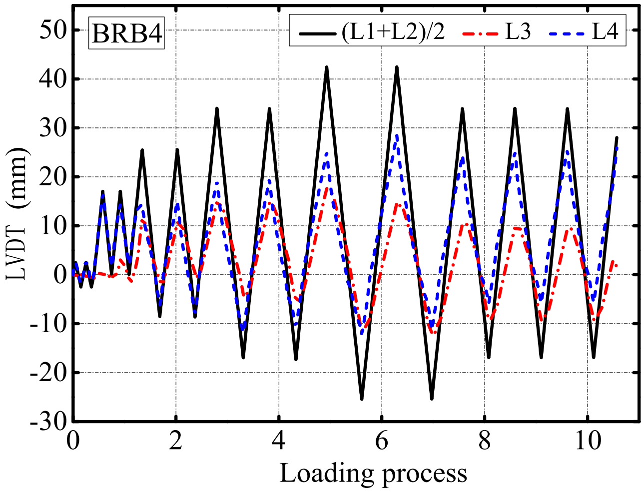

FIGURE 7 The relationship among (L1 + L2)/2, L3 and L4

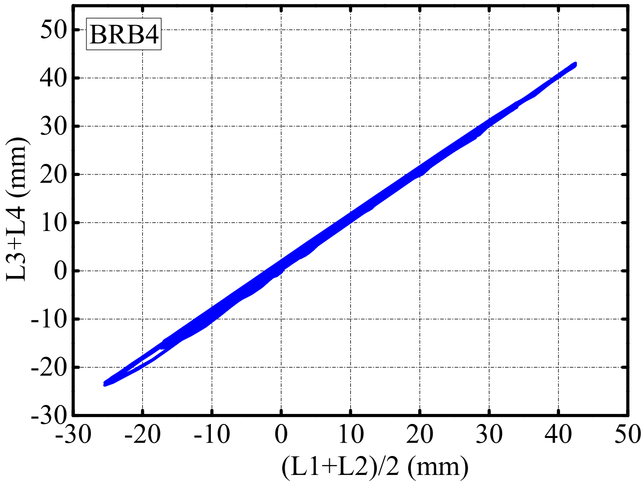

FIGURE 8 The relationship between (L1 + L2)/2 and L3 + L4

After the test, the specimens were disassembled by removing the high-strength bolts. The surfaces of the core of all the specimens were partly polished around the high-mode buckling wave crests, as shown in Figure 10.

3.3 | Equivalent viscous damping ratio

The equivalent viscous damping ratio of the BRB is defined as Equation 2, according to the Chinese seismic design code for buildings GB5001-2010.[35]

$$\zeta = \frac{W_c}{4\pi W_s} = \frac{S_{ABCD} + S_{AFED}}{2\pi (S_{FHO} + S_{CGO})}, \tag{3}$$

where W_c is the energy dissipated in a cycle for a given displacement and $S_{ABCD} + S_{AFED}$ is the area surrounded by the hysteresis curve, as shown in Figure 11. W_s is the elastic strain energy for a given displacement, and $S_{FHO} + S_{CGO}$ is the summation of the △FHO and △CGO areas.

The equivalent viscous damping ratio of specimens at different strain amplitudes were obtained and are presented in Table 1. It was found that the equivalent viscous damping ratio increased gradually as the total strain amplitude increased. The equivalent viscous damping ratio of all specimens exceeded 0.4 at each total strain amplitude.

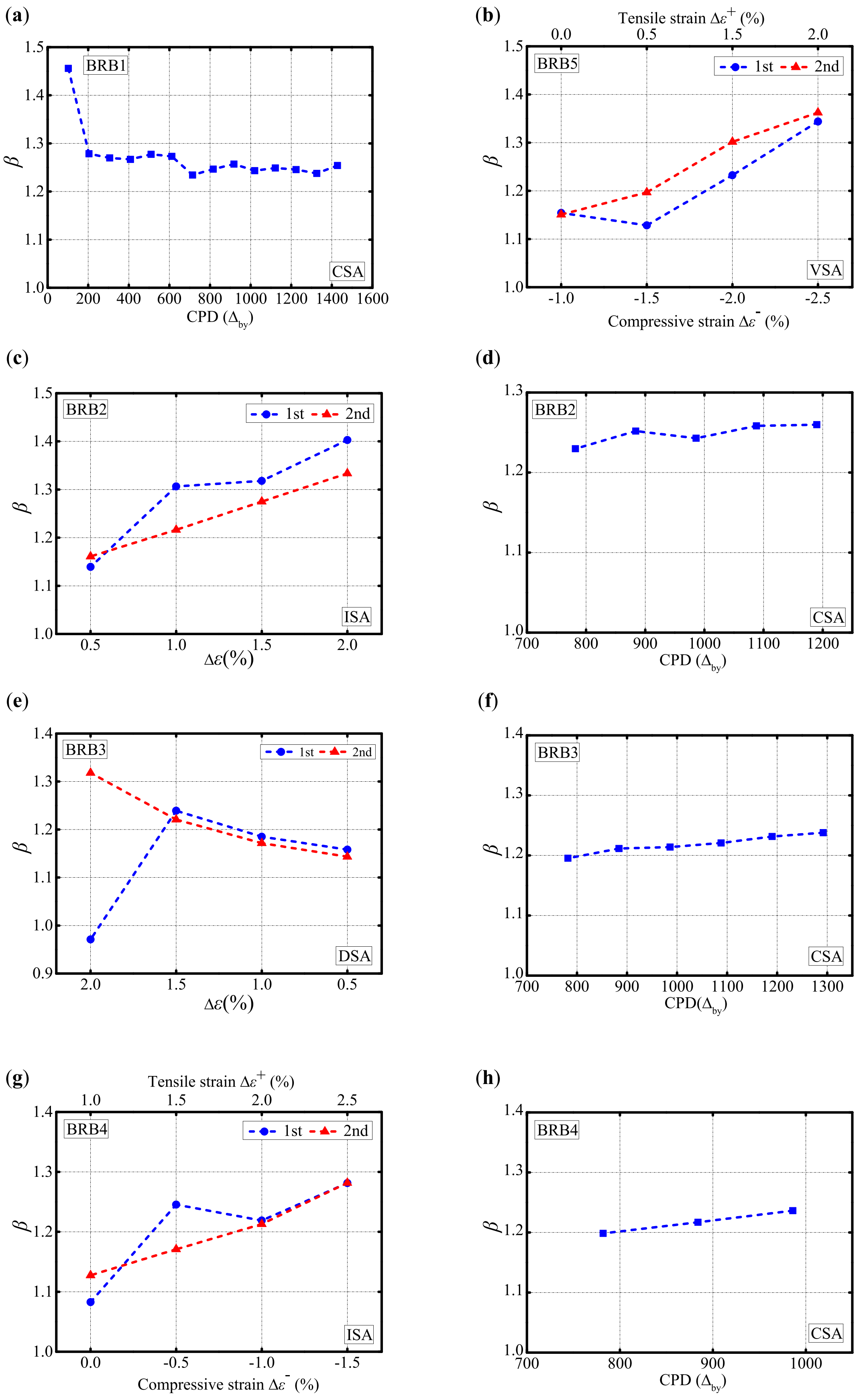

FIGURE 9 The compression strength adjustment factor for specimens at each strain level and different CPD values (a) Specimen 1; (b) Specimen 5; (c) Specimen 2-ISA; (d) Specimen 2-CSA; (e) Specimen 3-DSA; (f) Specimen 3-CSA; (g) Specimen 4-ISA; (h) Specimen 4-CSA

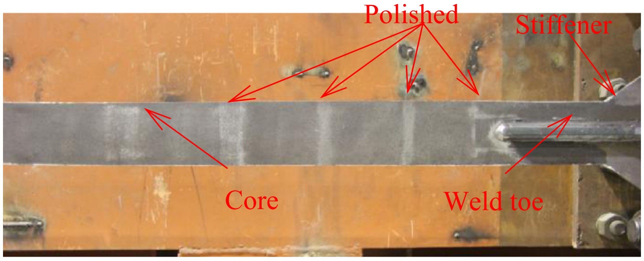

FIGURE 10 The polished surface of core

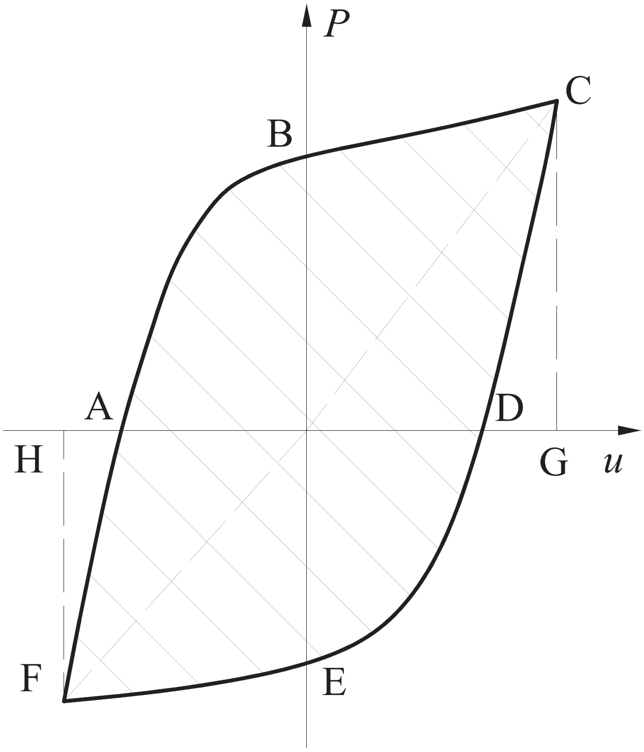

FIGURE 11 Calculation of the equivalent ratio of critical viscous damping

TABLE 1 Equivalent viscous damping ratio

Specimen number	Total strain amplitude: $\Delta\varepsilon = \Delta\varepsilon^{+} + \lvert\Delta\varepsilon^{-}\rvert$ 1.0%	2.0%	3.0%	4.0%
1	–	–	0.475	–
2	0.435	0.471	0.473	0.475
3	0.421	0.463	0.465	0.468
4	0.428	0.465	0.467	0.470
5	0.437	0.469	0.475	0.477

3.4 | Failure modes

The test results of five specimens showed that the fracture was initiated from the edge of middle stoppers, as shown in Figure 12. The fracture phenomenon of each core can be easily observed from the space between the bolts without disassembling the braces, as shown in Figure 12f. Residual stress and stress concentration due to the weld toes was less likely to occur in these specimens; hence, the low-cycle fatigue

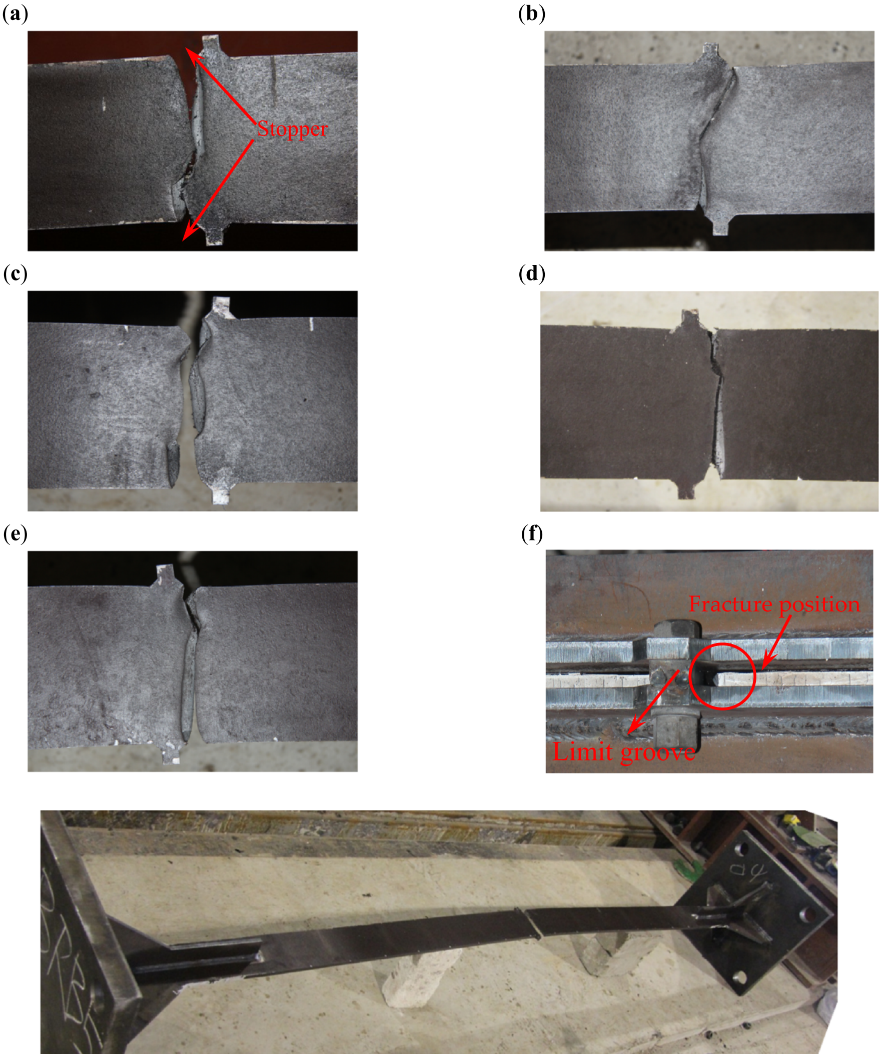

(g) The core after fracture

FIGURE 12 Failure modes of specimens: (a) Specimen 1; (b) Specimen 2; (c) Specimen 3; (d) Specimen 4; (e) Specimen 5; (f) Fracture position; (g) The core after fracture

performance of specimens was improved. No cracking occurred at the weld toes at the base of stiffeners, which indicates that the smoothing method was reliable and effective.

Because the stoppers were located at the middle of the core, the compressive stress in the end section was the largest, and the compressive stress in the middle section was the smallest when the core was pressed due to the existence of friction; thus, the expansion of the end section was larger than that of the middle section. When the core was pulled, a friction force between the core and restraining system unloaded quickly, and at this time, the axial tensile force on each section was equal. Due to the difference in cross-sectional size caused by pressure, the tensile stress at the end section was smaller than that at the middle section, which led to the middle section being smaller than the end section. Due to the reciprocating effect, the middle section was more likely to be damaged first, without considering the stress concentration caused by the stoppers. Significant reduction of the cross-sectional size was also observed at the middle of the core for all specimens; while and increment of the cross-sectional size at end section.

After the test, the bolts were disassembled, and the width of the core's yield segment was measured along the axis of the core (Points A–S in Figure 13). The width of Point J is the width of the fracture surface, regardless of the size of stoppers. The core residual transverse deformations were calculated based on the initial width bc = 100 mm. The core plate residual transverse deformations are shown in Figure 14. The experimental results indicate that the middle region of the yield segment shrank, and the end region of the yield segment expanded considerably. To some extent, this was due to the influence of friction.

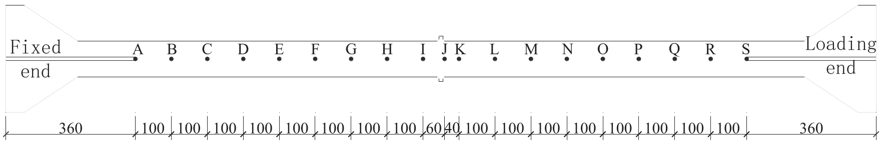

FIGURE 13 The position of the measuring points

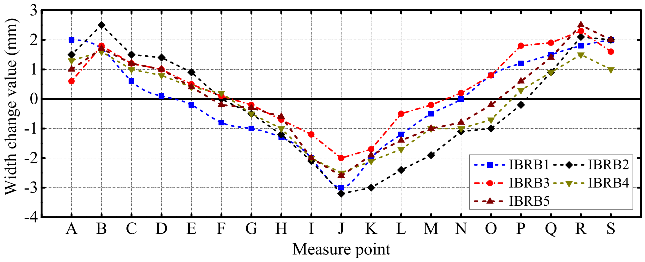

FIGURE 14 Residual transverse deformation of core

3.5 | Deformation of restraining system

Three strain gauges were installed in the middle section of the web, and the other three strain gauges were attached to the panel near the critical points of the channels and panels. The restraining units were made of Chinese Q345-B steel, and the yield strain can be calculated according to the yield stress and elastic modulus obtained from the material tests, that is, the yield strain was equal to 0.0019. The maximum strain of the six strain gauges along the longitudinal and transverse direction reached 0.00057 and 0.00025, respectively, less than the yield strain, which generally indicates little participation of the restraining system in load resisting.

LVDT5 and LVDT6 were used to measure the lateral displacement of the restraining system's midpoint along the core thickness and width, respectively. Two of the LVDTs were dropped during the test of the first three specimens, the recorded data was incomplete; thus, only the lateral displacement results of Specimens 4 and 5 were given. The maximum lateral deformation did not exceed 3 and 6 mm along the core thickness and width, respectively. During the test, no global instability was detected in any of the specimens, and the lateral displacements of restraining system's midsection were negligible. The results of the six strain gauges and two lateral LVDTs show that the design of the restraining system is reasonable.

3.6 | Multi-wave buckling deformation

During the test, the actuator was paused at the first cycle of each peak compressive strain to measure the deformation state of core, and the monitoring points are shown in Figure 2 of Points a to f. Taking Specimen 2 as an example, the deformation process of the whole loading process is shown in Figure 15, and the typical core deformation is shown in Figure 16.

The deformation of the core was not uniform along its axis, and the deformation curve was not a pure sine or cosine curve. The contact between the core and the restraining system not only included the point of contact but also the contact line, which appear alternately. For the specimen with the ISA loading protocol, the number of core buckling waves increased and the wavelength became shorter while the distribution became more uniform with the increase of the compressive strain.

The measured buckling wave numbers of the five specimens at each monitoring point are presented in Table 2. Because of the line contact, the wave number could not be accurately determined. It was assumed that each line contact segment was still a contact point in the calculation. For Specimen 3, the core first underwent a large compressive strain and then carried a calculation. For Specimen 3, the core first underwent a large compressive strain and then carried a gradually reduced compressive strain. Because the residual deformation cannot completely restore under tension, the waveform will transform based on the deformation state of the larger compressive strain. Even if the subsequent compressive strain is smaller, the wave number will not be less than that of the previous larger compressive strain. The minimum buckling wavelength is related to the maximum compressive force of the core, independent of the loading history. For the specimens with different loading protocols, the buckling wave numbers were not the same even under the same compressive strain amplitude, which means the corresponding compressive force may have been different under cyclic loading. For instance, under the same compressive strain amplitude of 1.5% for Specimens 1–3 whose

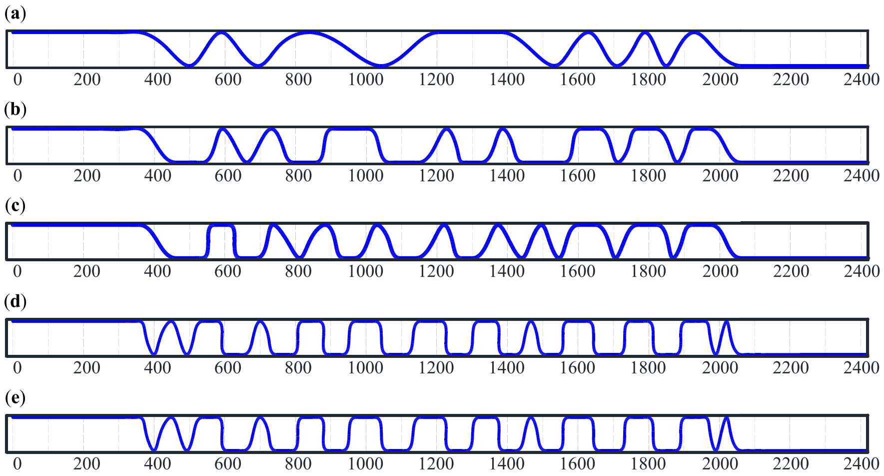

FIGURE 15 Core deformation process of Specimen 2 (test): (a) Point b ($\Delta\varepsilon_c^- = -0.5\%$); (b) Point c ($\Delta\varepsilon_c^- = -1.0\%$); (c) Point d ($\Delta\varepsilon_c^- = -1.5\%$); (d) Point e ($\Delta\varepsilon_c^- = -2.0\%$); (e) Point d1 ($\Delta\varepsilon_c^- = -1.5\%$)

FIGURE 16 Typical deformation of core shape

TABLE 2 Comparison of the deformation

Specimen number	Point	Compressive strain	P(kN)	n_t	n_c	n_f	l_{ct} (mm)	l_{cc} (mm)	l_{cf} (mm)
IBRB1	d	1.5%	426	9.5	9.1	10.5	179	186	162
IBRB2	b	0.5%	331	6.5	8.0	6.5	262	211	262
	c	1.0%	387	8.5	8.7	9.5	200	195	179
	d	1.5%	456	10.5	9.4	9.5	162	180	179
	e	2.0%	543	12.5	10.3	11.5	136	165	148
IBRB3	b	0.5%	360	12.5	8.4	12.5	136	203	136
	c	1.0%	428	12.5	9.1	12.5	136	186	136
	d	1.5%	465	11.5	9.5	11.5	148	178	148
	e	2.0%	354	8.5	8.3	8.5	200	204	200
IBRB4	a	0%	315	4.5	7.8	5.5	378	217	309
	b	0.5%	373	7.5	8.5	9.5	227	199	179
	c	1.0%	426	9.5	9.1	12.5	179	186	136
	d	1.5%	515	11.5	10.0	12.5	148	169	136
IBRB5	c	1.0%	329	6.5	8.0	7.5	262	212	227
	d	1.5%	360	9.5	8.4	9.5	179	203	179
	e	2.0%	442	11.5	9.3	10.5	148	183	162
	f	2.5%	532	12.5	10.2	11.5	136	167	148

loading protocols are symmetrical, the wave buckling numbers are 9.5, 10.5, and 11.5, respectively. However, the corresponding compressive forces for Specimens 1–3 are 426, 456, and 465 kN, respectively (see Figure 6). As the wave buckling number increases, so does the compressive force.

The buckling wave numbers of the core under axial pressure have a great influence on the performance of the restraining system. If the contact points between the core and the restraining system cannot be calculated accurately, the constraint system cannot be reasonably designed. Therefore, the measured core wave numbers were compared with the theoretical calculation results. Under the axial pressure P, the theoretical average wavelength of the core can be calculated as follows[23]:

$$l_{cc} = 2l_0 = 4\pi\sqrt{\frac{0.06E_cI_c}{P}}, \tag{4}$$

where l_{cc} is the average wavelength; $0.06E_cI_c$ is the effective bending stiffness, and the double modulus theory has been adopted to take the loading and unloading responses into account.[36] The measured deformation state, the theoretical results, and the finite element method (FEM) results are compared in Table 2. l_{ct} is the measured average wavelength, and l_{cf} is the FEM average wavelength. n_t is the measured wave number, n_c is the theoretical wave number, and n_f is the FEM wave number. The results show that the experimental results were in good agreement with the theoretical results; therefore, the contact points between the core and the restraining system can be calculated according to Equation 4.

4 | FINITE ELEMENT ANALYSIS

4.1 | Finite element model

4.1.1 | Simulation method

The general finite element (FE) software ABAQUS was adopted to simulate the performance of the five specimens tested in this research. The results were compared with the experimental results. The full Newton–Raphson method was used when solving nonlinear equations in the analysis. In addition, an initial geometrical deformation of 3/1000 of the BRB length is set for the FE models of the core steel according to the measured average data of the five specimens. When a brace is pressed, the core will buckle and interactions between the core and restraining system (e.g., the process of attachment, attachment disappearance and reattachment of the core and restraining plane) can cause severe computational instability. For this reason, an automatic stabilization factor using a quite small damping coefficient of 2.0E-4 was specified to simplify the convergence in the static analysis process of the BRB. The reference points RP1 and RP2 were established at the left and right ends of the model; furthermore, the reference points were coupled to the corresponding end surfaces. During the simulation, six degrees of freedom for reference point RP1 were fixed, and only the axial displacement was allowed for RP2. The loading protocols are the same as those in the test.

The FE model duplicates the specimen setup and protocol in the test, as shown in Figure 17. The model includes the core, stiffeners, panels, channels, high-strength bolts and limit grooves. All the specimen parts are modeled using eight-node solid elements (C3D8R), which can better simulate the contact property. The core is divided into seven elements over its width and two in the thickness direction. Stiffeners, panels, channels and limit grooves are divided into two elements over the core's thickness, and the global element size is 20 mm. The gap between the core and restraining system is the same as that of the specimens.

During the actual testing, high-strength bolts were used to connect two restraining units together, and the gap between the core and restraining system was fixed by annular gaskets. To facilitate the analysis, a single high-strength bolt and annular gasket are simplified as cylinders in the model with a diameter equal to that of the screw and a height equal to that of the annular gasket. The cylinders and limit grooves are connected to the two panels to tie in or simulate the interaction type, regardless of the bolt holes. Bolts were not loose in the test, so it is reasonable to use this connection method. The simulated tie-in interaction simulation is also used between panels and channels, stiffeners and core.

The interaction between the core and its restraining system includes the normal force and the tangential frictional force. The 'hard contact' interface property is set in the normal direction, and the Coulomb friction model is employed to simulate tangential behavior. When the normal contact pressure became negative or zero, the two contact surfaces were separated. The corresponding surfaces of panels, cylinders and limit grooves are defined as the main surfaces, and the core surfaces are defined as the slave faces. The test results of the five specimens showed that the compression strength adjustment factors were not the same, so the friction coefficient of each specimen had to be determined through several trials during the FE simulation process. The smaller the difference was in the ultimate compression strength between the simulation and the test, the more accurate the friction coefficient would be. The optimal coefficient of friction from Specimens 1 to 5 was 0.12, 0.18, 0.15, 0.15, and 0.22, respectively.

4.1.2 | Material model

As shown in a previous study, the mechanical behavior of steel under cyclic loading is different from that under monotonic loading. The core made of Q235-B steel was directly subjected to the cyclic load, whereas the restraining system made of Q345-B steel can only bear the normal force

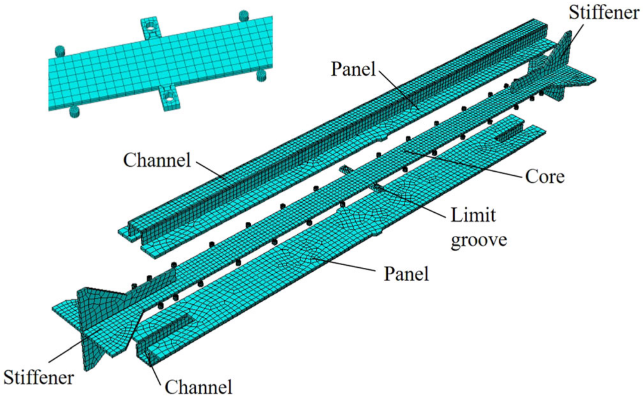

FIGURE 17 Finite element model of the specimens

and tangential friction force at the contact points. In this paper, the Chaboche model[37] was used for Q235-B steel. For the Q345-B steel, the authors adopted the isotropic hardening model. Due to the bolts' high axial stiffness, an elastic model was applied to high-strength bolts. Young's modulus and Poisson's ratio were selected to model 200 GPa and an 0.3 ratio, respectively.

The Chaboche model[37] is a combined hardening model with both isotropic hardening and kinematic hardening components. The actual stress beyond the elastic stage is a sum of the isotropic hardening and kinematic hardening components. The yield surface size describes isotropic hardening, and the backstresses describe kinematic hardening.

Isotropic hardening assumes that the yield surface is uniformly expanded in the loading process without any distortion or translation. The size of subsequent yield surface can be obtained as follows[38]:

$$\sigma_y = \sigma_{y0} + R = \sigma_{y0} + Q_\infty\left(1 - e^{-b\varepsilon_{eq}}\right), \tag{5}$$

where σ_y is the size of the subsequent yield surface; σ_{y0} is the yield stress at zero equivalent plastic strain; R is the change of the yield surface size, and the initial value of R is zero; b gives the rate at which the size of the yield surface changes as the plastic strain increases; Q_∞ is the maximum change of the yield surface, and ε_{eq} is the equivalent plastic strain.

Based on the kinematic hardening, it is assumed that the translation of yield surface in the stress space is rigid without rotation and expansion, so the size, shape, and orientation of the yield surface remain unchanged. The total backstresses provided by ABAQUS[39] are

$$\alpha = \sum_{k=1}^{n} \frac{C_k}{\gamma_k}\left(1 - e^{-\gamma_k \varepsilon_{eq}}\right), \tag{6}$$

where α is the total backstress, which indicates the movement of the yield surface; n is the total number of backstresses; C_k and γ_k are the model parameters used to define the shape of the ith backstress curve, and ε_{eq} is the equivalent plastic strain. The initial values of all the backstresses are zero.

The Mises yield function is adopted since it is generally accepted for metals. The yield function is given as

$$f = \sqrt{\frac{3}{2}(\mathbf{S} - \boldsymbol{\alpha}) : (\mathbf{S} - \boldsymbol{\alpha})} - (\sigma_{y0} + R) = 0, \tag{7}$$

where $\mathbf{S}$ and $\boldsymbol{\alpha}$ are the deviatoric stress, and the total backstresses, σ_{y0} and R, are the initial yield stress and isotropic hardening component, respectively.

Shi et al.[40] conducted material tests on different kinds of steel, and the parameters of the Chaboche model were fitted. This method requires too many material tests under different loading protocols. When the specimen is compressed, it is easy to lose stability, which makes it difficult to obtain the material parameters. Based on a previous study[41] in which the yield stress under compression in every cycle is close to the initial yield stress σ_{y0} (as shown in Figure 18), Jia et al.[42] proposed a method to obtain the parameters of the Chaboche model by using only tensile coupon test. Using this method, the size of the subsequent yield surface, $\sigma_{y0} + R$, can be obtained using this calculation

$$\sigma_{\text{mono}} = \sigma_{y0} + 2R. \tag{8}$$

From Equation 12, the following formula can be obtained in a uniaxial stress state

$$\sigma_{\mathrm{mono}} - \alpha = \sigma_{y0} + R, \tag{9}$$

where σ_{mono} is the post-yield uniaxial stress of the monotonic true stress-true strain curve.

Clearly, the above statement indicates that the isotropic hardening component is the same as the kinematic hardening component in the true stress-true strain curve obtained from the monotonic coupon test. ABAQUS can automatically fit the Chaboche model parameters. Thus, C_i and γ_i are related to kinematic hardening and can be calibrated by inputting the monotonic true stress-true plastic strain data. The isotropic hardening component, R, can be obtained from Equation 6. The model parameters related to the isotropic hardening, that is, the maximum change of the yield surface, Q_∞, and the rate at which the size of the yield surface changes as the plastic strain increases, b, can be obtained by inputting the size of the subsequent yield surface and true plastic strain.

The uniaxial tensile coupon made of Q235-B steel was tested, and the parameters were calibrated through the method mentioned above; the parameter details are provided in Table 3. The true stress–true strain relationship obtained from the tensile coupon test and that obtained from the numerical simulation using the parameters given in Table 3 are plotted in Figure 19, which clearly shows the results to be well matched, proving the validity of the material model and the correctness of the parameters.

4.2 | Numerical results

4.2.1 | Hysteretic loops

The hysteresis curves obtained by FE simulation were compared with those obtained from the test, as shown in Figure 6, where the vertical axis was the axial force, and the horizontal axis was the axial deformation, with a positive tension and negative compression. The results showed that the elastic stiffness, post-yield stiffness and hysteresis response obtained from numerical simulation were in good agreement with the experimental results. The FE model can use the friction coefficient to better simulate the maximum compressive force. However, the friction coefficient in this study was affected by many factors, which made it difficult to accurately determine the maximum compressive force. The greater the friction coefficient was, the greater the compression strength adjustment factor will be. For that reason, when specimens reached the maximum compressive strain and began to carry out reverse loading, the compressive force went through a rapid descent stage due to the rapid unloading of the friction force. This phenomenon can be observed in hysteretic loops from both the test and FE analysis.

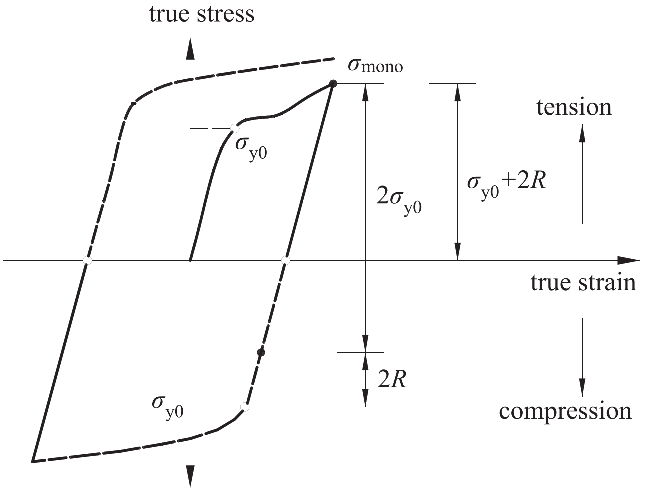

FIGURE 18 Relationship between monotonic and cyclic true stress–true strain

TABLE 3 Chaboche model parameters

σ_{y0} (MPa)	C_1 (MPa)	γ_1	C_2 (MPa)	γ_2	C_3 (MPa)	γ_3	Q_∞ (MPa)	b
282	295	0	327	14	1270	15	110	8

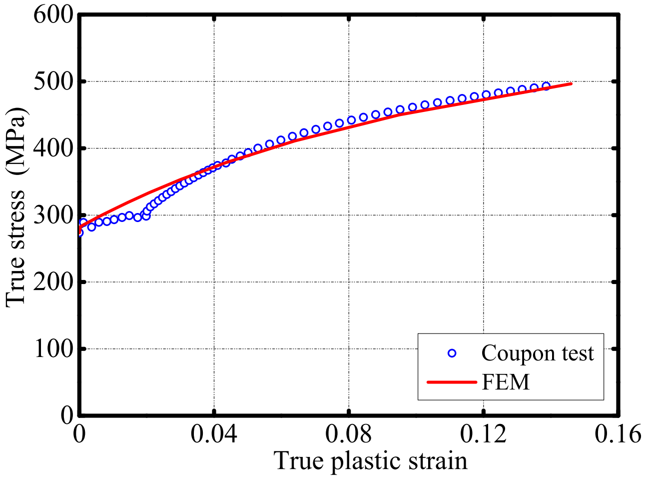

FIGURE 19 Coupon test and numerical material model

4.2.2 | Multi-wave buckling deformation

During the test, the deformation process of the core was monitored. Taking Specimen 2 loaded with standard protocol as an example, the deformation process of the core is shown in Figure 20, and the monitoring points are shown in Figure 20b. Typical deformation of the core is shown in Figure 21. When the core reached the first +8.5 mm displacement and then reversed loading, the core was quickly unloaded and then turned into compression. With the increase of the compressive displacement, the axial compressive force increased rapidly until yield, and the core's waveform also changed rapidly in a short time. In Figure 20b–e, the average wavelength decreases and the wave number of the core increases with the increase of the axial compressive displacement. The compressive strain in Figure 20d was the same as that at point d1 in Figure 20e, but the deformation state was different, since the buckling deformation could not recover completely when the core was in tension. Therefore, when the core underwent a larger compressive strain and then underwent a smaller compressive strain, the core waveform transforms based on the previous larger compressive strain. The numerical simulation results showed that the variation tendency of the wave of the core was consistent with the experimental results.

The results comparing the buckling wave numbers of the core at each monitoring point obtained from the test and numerical simulation are shown in Table 2. The results indicate that the FEM can well predict the buckling wave numbers of the core, even though deformation shape at each point was not exactly the same. Under the action of the cyclic reciprocating load, the final core thickness is shown in Figure 22 where the end is clearly larger than the middle due to the influence of friction.

5 | DAMAGE ASSESSMENT METHOD

Many experimental results show that BRB has good plastic deformation ability, no universally accepted method exists that can predict the cumulative plastic deformation ability of BRB. It is difficult to accurately assess the damage state of BRB after an earthquake because the damage state of the core is affected by the deformation history. When a BRB core does not fracture, the damage state of the core must be evaluated to confirm or reject the need for structural reinforcement and BRB replacement.

5.1 | Subsection

In general, the component damage model consists of a single-parameter damage criterion and two parameter damage criteria. Thus, damage index D with a value equal to 1 corresponds to failure, and a value less than 1 indicates non-failure. Failure in single parameter damage criterion is defined as the first breakthrough past the damage parameter to its threshold; therefore, the single parameter damage model can be expressed as

$$D=\left(\frac{\delta_m-\delta_y}{\delta_u-\delta_y}\right)^m, \tag{10}$$

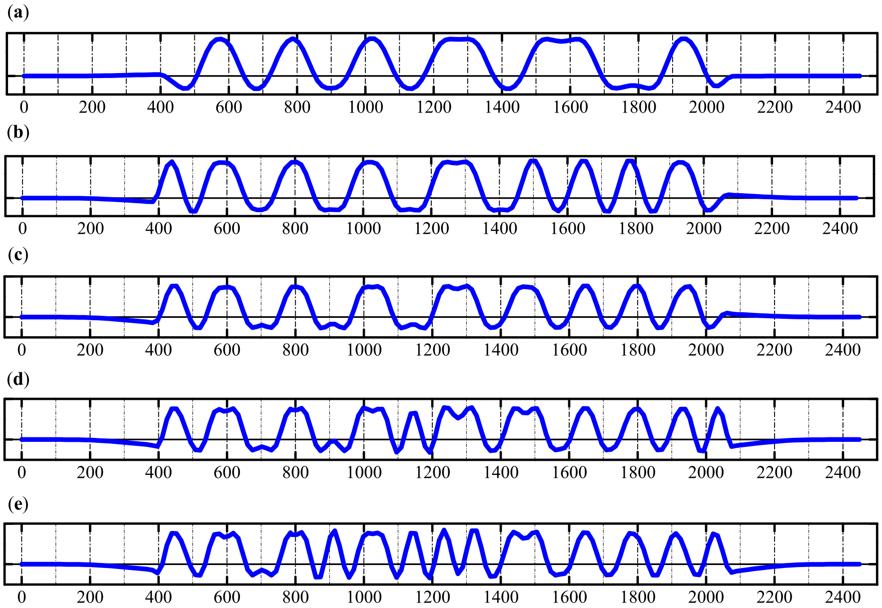

FIGURE 20 Core deformation process of Specimen 2 (FEM) (a) Point b ($\Delta\varepsilon_c^- = -0.5\%$); (b) Point c ($\Delta\varepsilon_c^- = -1.0\%$); (c) Point d ($\Delta\varepsilon_c^- = -1.5\%$); (d) Point e ($\Delta\varepsilon_c^- = -2.0\%$); (e) Point d1 ($\Delta\varepsilon_c^- = -1.5\%$)

FIGURE 21 Typical deformation of the core

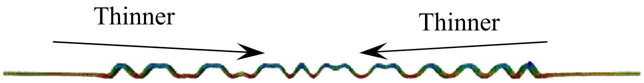

FIGURE 22 The final thickness of core

where *D* is the damage index; δ_m is the maximum axial deformation that occurs due to a seismic loading; δ_u is the ultimate axial deformation capacity when subjected to a monotonic loading; δ_y is the axial yield deformation, and *m* can be selected according to the actual situation, generally preferred as 1.

The single parameter model that considers only the maximum deformation cannot consider the effect of cumulative damage. To overcome the disadvantages of the single parameter model, the two parameter damage criteria were recommended. Park and Ang[31] proposed a damage model that considers both the maximum deformation and the cumulative energy dissipation. In this case, the damage index is calculated as follows:

$$D = \frac{\delta_m}{\delta_u} + \frac{\beta}{F_y \delta_u} \int \mathrm{d}E_h, \tag{11}$$

where F_y is the axial yield force; $\int \mathrm{d}E_h$ is the total absorbed hysteretic energy; and β is a non-negative term that serves as a model parameter. It is assumed that the load–displacement curve of BRB is perfectly elastic–plastic; thus, the simplified Park–Ang damage model can be rewritten as

$$D = \frac{1}{\mu_\mathrm{u}} (\mu_\mathrm{m} + \beta \cdot CPD), \tag{12}$$

where μ_u is the ultimate ductility capacity, which can be expressed as the ratio of ultimate tensile strain to yield strain. The ultimate tensile strain of the core was 29.5% based on the results of the material test; μ_m is the value of the maximum ductility demand up to the point in the deformation history at which the damage index is determined; *CPD* is the cumulative plastic deformation at the point in the deformation history at which the damage index is determined; and β is a deterministic model parameter that controls the relative amount of damage attributed to maximum deformation versus cumulative deformation. μ_u can be obtained from the material test of the core. β can be acquired from the cyclic test results of BRBs under different loading protocols if the damage index is 1 when the core fractures. Because β is affected by the deformation history and cannot be accurately determined, the average value can be simply taken.

Based on the simplified Park–Ang damage model, the damage evolution process of the five specimens can be obtained, as shown in Figure 23. It is assumed that the damage index was 1 when each specimen was fractured; thus, the damage index is roughly linear with the cumulative plastic deformation.

5.2 | Performance levels

After calculating the damage index of BRB, it is necessary to determine its performance level. Wang[43] divided the steel structure into six different performance levels according to the damage index, as shown in Table 4.

It is recommended that the BRB should be replaced in time if the performance level meets or exceeds medium damage, that is, if the damage index *D* is greater than 0.25. If the damage index *D* does not exceed 0.25, the remaining plastic deformation capacity and remaining stiffness of the BRB must still be recalculated as follows

$$K_r = (1-D)K_0, \tag{13}$$

$$RC = (1-D)\cdot TC, \tag{14}$$

where K_r and K_0 are the remaining stiffness and initial stiffness, respectively; RC and TC are the remaining and total plastic deformation capacity, respectively. After determining the remaining deformation capacity and remaining stiffness of the BRB, it is necessary to reevaluate the seismic bearing capacity of the structure.

5.3 | Damage assessment process

After the earthquake, the process of assessing BRB damage is proposed as follows:

1. BRB is surveyed to obtain the relevant damage information. If the core is fractured or necking occurs, or the overall stability failure, connection failure and other obvious damage phenomenon are observed, it needs to be replaced directly.

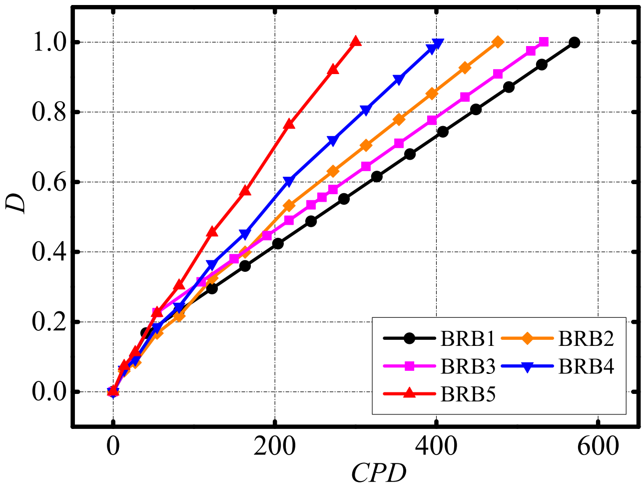

FIGURE 23 Damage evolution process

TABLE 4 Performance levels

Performance levels	Damage index
Keep intact	0–0.1
Minor damage	0.1–0.25
Medium damage	0.25–0.45
Heavier damage	0.45–0.65
Serious damage	0.65–0.9
Completely destroyed	>0.9

2. If the damage state of the BRB cannot be evaluated from its appearance, the deformation history of the BRB should be obtained based on the deformation recorder installed on the brace. And then the damage index is calculated based on the single parameter damage criterion or the two parameter damage criteria. If the deformation history of the BRB cannot be obtained, the maximum deformation of the core can be measured according to the friction traces between the core and the restraining system, so that the single parameter damage model can be used to evaluate the damage state of the core.
3. If the corresponding performance level of the BRB exceeds the medium damage, this indicates the plastic deformation capacity of the BRB decreased by 25% at least compared to the original BRB. Considering the safety redundancy, it is recommended to replace the BRB. For the BRB without replacement, the remaining stiffness and remaining energy dissipation capacity should be corrected to reevaluate the seismic bearing capacity of the structure.

6 | CONCLUSIONS

A new inspectable all-steel assembled BRB was proposed. The restraining system consists of two identical restraining units which were connected by high-strength bolts and the gaps were fixed by corresponding annular gaskets. Channels were used to strengthen the out-of-plane stability and can be replaced by other cross-section members that can be rectangular or flat. Cyclic tests were conducted on five specimens with different protocols to investigate the mechanical performance of the new BRB. Additionally, FE analyses were carried out to explain the tests results. The main results were summarized as follows:

1. The deformation state of the core can be observed without disassembling the restraining system during the test, and the fracture location can be obtained from the space between bolts. After the earthquake, it is easy to evaluate the damaged BRB and replace the core to protect the main structure.
2. Low-cycle tests showed five specimens with different loading protocols to exhibit stable and repeated hysteretic performance with CPD capacities reaching 571, 476, 533, 402, and 300 for Specimens 1 to 5, respectively. Thus, brace test specimens were able to achieve a cumulative inelastic deformation higher than the value of 200 times the yield deformation required by AISC seismic provisions; the failure mode of the BRB was the rupture of the core initiating from the edge of the midsection stoppers. There was no crack in the weld toes of the stiffeners, which indicated that the smoothing method was reliable and effective. When the hysteretic curve was stable, the maximum compression strength adjustment factors of Specimens 1 and 4 were below 1.3, whereas the other specimens had a maximum compression strength adjustment factor greater than the code limit of 1.3. For high-performance all-steel BRB, it is also advisable to provide debonding materials to get a higher low-cycle fatigue property.
3. The fine FE model can appropriately simulate the hysteretic performance of specimens, considering the friction coefficient and combining the hardening components. The multi-wave buckling deformation can be satisfactorily predicted by using FE analysis.
4. The results of testing and FEM indicated that the larger the compressive strain was, the more the high-mode buckling wave number would be for the specimen with ISA loading. The wave number would not decrease if the subsequent compressive strain was smaller than the previous one. This is because the residual deformation cannot completely restore under tension; thus, the waveform transforms on the basis of the deformation state of previous larger compressive strains. The deformation of the core was not uniform along the length. The experimental results were in good agreement with the theoretical results, so the number of contact points can be calculated using the theoretical formula in the design of the restraining system.
5. A damage assessment method was proposed to evaluate the working status of the BRB after the earthquake, which can provide confirmation as to whether the BRB should be replaced, thereby strengthening the performance appraisal of the post-earthquake structure.

FUNDING INFORMATION

This research was funded by Natural Science Foundation of Shanghai (grant number: 20ZR1461800) and the Intergovernmental International Scientific and Technological Innovation Cooperation Special Focus (under grant #2021YFE0112200).

CONFLICT OF INTEREST

All authors declare that they have no conflict of interest.

DATA AVAILABILITY STATEMENT

The data that support the findings of this study are available from the corresponding author upon reasonable request.

REFERENCES

[1] JSSI, Report of response-controlled buildings, Japan Society of Seismic Isolation (JSSI) Investigation Committee, Tokyo, **2012**.
[2] K. Kasai, A. Mita, H. Kitamura, K. Matsuda, T. A. Morgan, A. W. Taylor, *Earthq. Spectra* **2013**, *29*(1_suppl), 265.
[3] L. Xie, M. Cao, N. Funaki, H. Tang, S. Xue, *J. Asian Archit. Build. Eng.* **2015**, *14*(1), 181.
[4] M. Cao, L. Xie, H. Tang, N. Funaki, S. Xue, *J. Asian Archit. Build. Eng.* **2016**, *15*(2), 303.
[5] Q. Xie, *J. Constr. Steel Res.* **2005**, *61*(6), 727.
[6] P. Pan, W. Li, X. Nie, K. Deng, *J. Sun. Struct. Des. Tall Spec. Build.* **2017**, *26*(4), e1335.
[7] K. Kimura, Y. Takeda, K. Yoshioka, Summaries of technical papers of Annual Meeting of the Architectural Institute, Japan **1976**.
[8] N. Mochizuki, Y. Murata, N. Andou, Annual Meeting of the Architectural Institute of Japan, Japan **1980**.
[9] P. Clark, I. Aiken, K. Kasai, O. E. K. I. Kimura, Proceedings of 68th Annual Convention, Sacramento, USA **1999**.
[10] T. Takeuchi, J. F. Hajjar, R. Matsui, K. Nishimoto, I. D. Aiken, *J. Constr. Steel Res.* **2010**, *66*(2), 139.
[11] P. C. Lin, K. C. Tsai, C. A. Chang, Y. Y. Hsiao, A. C. Wu, *Earthq. Eng. Struct. Dyn.* **2016**, *45*(3), 339.
[12] Y. Gao, Y. Yuan, C. L. Wang, B. Zeng, L. Guo, *Struct. Des. Tall Spec. Build.* **2020**, *29*(4), e1702.
[13] D. H. Kim, C. H. Lee, Y. K. Ju, S. D. Kim, *Struct. Des. Tall Spec. Build.* **2015**, *24*(4), 243.
[14] C. C. Chou, S. Y. Chen, *Eng. Struct.* **2010**, *32*(8), 2108.
[15] B. N. Sridhara, 4th International Conference on Steel Structures and Space Frames, Singapore **1990**.
[16] M. Tada, S. Kuwahara, T. Yoneyama, *J. Struct. Constr. Eng.* **1993**, *445*, 151.
[17] Y. K. Ju, M. H. Kim, J. Kim, S. D. Kim, *Eng. Struct.* **2009**, *31*(2), 507.
[18] D. Piedrafita, X. Cahis, E. Simon, *J. Comas. Eng. Struct.* **2015**, *85*, 118.
[19] Y. Guo, L. Jiang, *Build. Struct.* **2010**, *40*(1), 30.
[20] J. P. Judd, I. Marinovic, M. R. Eatherton, C. Hyder, A. R. Phillips, A. Tola Tola, F. A. Charney, *J. Constr. Steel Res.* **2016**, *125*, 164.
[21] R. Tremblay, P. Bolduc, R. Neville, R. DeVall, *Can. J. Civ. Eng.* **2006**, *33*(2), 183.
[22] T. Usami, C. L. Wang, J. Funayama, *Earthq. Eng. Struct. Dyn.* **2012**, *41*(4), 643.
[23] F. Genna, P. Gelfi, *J. Struct. Eng.* **2012**, *138*(10), 1244.
[24] C. L. Wang, T. Usami, J. Funayama, *Eng. Struct.* **2012**, *41*, 167.
[25] S. A. R. Tabatabaei, S. R. Mirghaderi, A. Hosseini, *Eng. Struct.* **2014**, *77*, 143.
[26] A. C. Wu, P. C. Lin, K. C. Tsai, *Earthq. Eng. Struct. Dyn.* **2014**, *43*(3), 375.
[27] Q. Chen, C. L. Wang, S. Meng, B. Zeng, *Eng. Struct.* **2016**, *111*, 478.
[28] Y. Liu, C. S. Tsai, *Earthq. Resist. Eng. Retrofitting* **2015**, *37*, 54.
[29] T. Takeuchi, M. Ida, S. Yamada, K. Suzuki, *J. Struct. Eng.* **2008**, *134*(5), 822.
[30] B. M. Andrews, L. A. Fahnestock, J. Song, *J. Constr. Steel Res.* **2009**, *65*(8–9), 1712.
[31] Y. J. Park, A. H. S. Ang, *J. Struct. Eng.* **1985**, *111*(4), 722.
[32] T. Usami, C. Wang, J. Funayama, *12th East Asia-Pacific Conference on Structural Engineering and Construction (EASEC)*, Elsevier, Hong Kong, China **2011**.
[33] American Institute for Steel Construction, *AISC341–10. Seismic Provisions for Structural Steel Buildings*, American Institute for Steel Construction, Chicago **2010**.
[34] T. Broom, R. K. Ham, N. F. Mott, *Proc. R. Soc. A* **1957**, *242*(1229), 166.
[35] China Architecture & Building Press, *GB50011-2010. Code for Seismic Design of Buildings*, China Architecture & Building Press, Beijing **2010**.
[36] P. C. Lin, K. C. Tsai, K. J. Wang, Y. J. Yu, C. Y. Wei, A. C. Wu, C. Y. Tsai, C. H. Lin, J. C. Chen, A. H. Schellenberg, S. A. Mahin, C. W. Roeder, *Earthq. Eng. Struct. Dyn.* **2012**, *41*(5), 1001.
[37] J. Lemaitre, J. Chaboche, *Mechanics of Solid Materials*, Cambridge University Press, England **1994**.
[38] F. Zaverl, D. Lee, *J. Nucl. Mater.* **1978**, *75*(1), 14.
[39] Z. Q. Jiang, Y. L. Guo, X. A. Wang, B. Huang, *J. Zhejiang Univ-Sci. A.* **2015**, *16*(10), 781.
[40] Y. Shi, M. Wang, Y. Wang, *J. Constr. Steel Res.* **2011**, *67*(8), 1185.
[41] L. J. Jia, H. Kuwamura, *J. Struct. Eng.* **2014**, *140*, 2.
[42] L. J. Jia, T. Koyama, H. Kuwamura, *Front. Struct. Civ. Eng.* **2013**, *7*(4), 466.
[43] C. B. Wang, *Study on index system and analytical method for seismic identification of existing high-rise steel frames*, Tongji University, Shanghai **2007**.

How to cite this article: C. Wan, L. Xie, L. Li, S. Xue, H. Tang, L. Zhang, *Struct Design Tall Spec Build* **2022**, e1924. https://doi.org/10.1002/tal.1924